





Effects of light-ion low-fluence implantation on the pressure response of double-walled carbon nanotubes

G. R. Hearne ^{1,2,*} L. Kapesi ^{1,2,†} R. M. Erasmus,^{2,3} S. R. Naidoo ^{2,3} and R. Warmbier ^{1,2}

¹*Department of Physics, University of Johannesburg, P.O. Box 524, Auckland Park 2006, Johannesburg, South Africa*

²*DSI-NRF Centre of Excellence in Strong Materials, University of the Witwatersrand, Wits 2050, Johannesburg, South Africa*

³*School of Physics, University of the Witwatersrand, Wits 2050, Johannesburg, South Africa*



(Received 18 February 2020; revised 28 February 2021; accepted 4 March 2021; published 22 March 2021)

Low-fluence light-ion ($^{11}\text{B}^+$) medium-energy (150 keV/ion) implantation preprocessing of double-walled carbon nanotubes (DWCNTs) has been effected to “decorate” them with defects. These are intended to serve as nucleation sites for potential sp^3 interlinking between tube walls in close proximity, following on strong deformation of the tube cross sections under cold compression to 20–25 GPa in diamond anvil cells. The pressure response of such implanted DWCNTs has been monitored *in situ* using Raman spectroscopy, and compared with those of unimplanted reference DWCNTs. Pressure dependences of the G^+ mode frequency and D to G^+ band intensity ratio, and radial breathing modes, have been monitored. These Raman signatures show that some degree of mechanical softening occurs in the implanted tube bundles, without major disruption to tube integrity in both samples. Consequently, the collapse pressure to racetrack or peanut shaped cross-sectional profiles is lowered substantially, from $P_c \sim 18$ GPa in the reference tube bundles to $P_c \sim 11$ GPa in the implanted case. Defect structures also proliferate more readily in the implanted sample under pressure. Therefore, the light-ion low-fluence implantation lowers the threshold pressure for deformation of tube cross sections to high-curvature profiles decorated with defects. Considerations of whether irreversible sp^3 interlinking at low volume fractions is discerned in the Raman data from implanted tube bundles under compression, and the stability of such bonding is discussed.

DOI: [10.1103/PhysRevMaterials.5.033607](https://doi.org/10.1103/PhysRevMaterials.5.033607)

I. INTRODUCTION

Carbon nanotubes (CNTs) have been shown theoretically and experimentally to have remarkable thermal, mechanical and electrical properties at the nanoscale. This makes nanotubes the most promising reinforcements for lightweight, multifunctional composites with the potential to revolutionize several industries such as power generation, construction, renewable energy, automotive, aerospace, and the medical field, to mention but a few examples [1]. Gaining benefits from thermal and mechanical properties of CNTs has proved to be elusive. Strong sp^2 bonds hold the nanotubes axially while, in contrast, adjacent tubes or layers are held together by weak van der Waals forces [2]. This, in turn, results in one major drawback common to the nanostructures — poor nanotube linkages (tube-to-tube as well as wall-to-wall for multiwall nanotubes). As such, instead of strongly coupling one wall to the next and potentially “amplifying,” for example, their mechanical properties such as buckling strain resistance and high tensile strength, multiwall carbon nanotubes tend to have their walls slide over each other in a process known as “telescoping.” Hence, outstanding properties of CNTs that are valid for single isolated tubes are hard to exploit at macroscale. Tubes tend to slide past each other when in bundles and between

layers in multiwall nanotubes. This poor cross linkage renders CNT assemblages incapable of carrying any significant load and it is also not good for heat transfer.

Interlinks involving sp^3 bonding between tubular walls of CNTs, at an optimum level of a few % volume fraction, have been suggested to substantially enhance mechanical (and thermal) properties of the resultant interlinked CNT structures [3]. Previous studies, done more extensively on single-wall carbon nanotubes (SWCNTs), have shown that both ion/electron irradiation and separate high pressure (HP) processing of CNTs have the potential of inducing interlinking between the CNT walls [4–8]. However, within appropriate high pressure limits, the changes induced by high pressure alone are usually reversible upon recovery to ambient pressure [4]. Otherwise, other carbon structures different from the starting CNTs are obtained from pressurization [4]. On the other hand, ion implantation that can induce meaningful interlinking results in excessive damage and subsequent loss or reduction in the mechanical properties observed on isolated CNTs [7,9–11].

Our main goal is to investigate and establish conditions for irreversible sp^3 interlinking in double-walled carbon nanotubes (DWCNTs), outer-to-outer wall inter-DWCNT links, and outer-to-inner tube intra-DWCNT links. To this end we deployed boron light-ion implantation preprocessing for defect decoration of tube surfaces, followed by HP processing in a diamond anvil cell (DAC). Sparse defects from low-fluence implantation may not induce sp^3 bonding directly, but they can act as nucleation sites for such bonding to be facilitated

*Corresponding author: grhearn@uj.ac.za

†Corresponding author: kapesiltk@gmail.com

upon HP processing that renders deformed high-curvature tube local environments known to favor sp^3 interlinking [12]. Our study aims to determine the minimum tailored pressure conditions for potential sp^3 bond formation without significantly altering other attractive properties of the DWCNTs.

We deployed Raman spectroscopy probing at *in situ* high pressure on both unimplanted and implanted DWCNT samples in DACs at room temperature to track structural-deformational changes and any different bonding characteristics and compare sample responses under cold compression.

The paper is organized as follows. Experimental methodology and measurement protocols are given in Sec. II. Results and discussions are presented in Sec. III, which is divided into four parts: Subsection A compares the high-pressure evolution at room temperature of Raman spectra of both starting unimplanted and implanted nanotubes. Subsection B deals with the collapse pressures of the DWCNTs. Subsection C considers defect proliferation under pressure in the DWCNTs. Subsection D considers the Raman spectra of the samples recovered to ambient conditions from high pressure. A summary of research findings and conclusions are given in Sec. IV.

II. EXPERIMENTAL METHODS

Double-walled CNTs (Sigma-Aldrich product no. 755168) were loaded into two separate DACs of the piston-cylinder [13] and Merrill-Bassett [14] types. Stainless steel gaskets, with a starting thickness of 250 μm , were preindented down to a thickness of 50 μm . A 200- μm -diameter sample cavity was then spark drilled at the center of a preindentation. One DAC contained unmodified starting DWCNT material, acting as a reference. The second DAC had the ion-implantation preprocessed DWCNTs. In both DACs, two to three ruby balls were placed within the central two-thirds of the area of the sample cavity for pressure measurements using the pressure shift of the ruby fluorescence R_1 line. The pressure distribution within the DAC cavity was monitored by comparing the pressure measured from each ruby placed at a particular position in the cell. As the goal of this work was to promote interlinking between individual CNTs, no pressure transmitting medium (PTM) was used, to avoid having any barrier between individual tubes.

Visible-Raman spectroscopy (VIS-Raman) measurements were done on a WITec Alpha 300R Confocal Raman system using a 532-nm laser excitation wavelength. A 600-line per mm grating in the large-area-scan mode of the WITec Alpha 300R Confocal Raman spectrometer was used to disperse the backscattered light onto a charge-coupled device (CCD) detector. The instrumental resolution was $\sim 4\text{ cm}^{-1}$. The laser power at sample was 1.3 mW. Due to sample inhomogeneity it was necessary to have an average spectrum representative of each pressure point (see the Supplemental Material [15], Sec. S1). To this end four $10\text{ }\mu\text{m} \times 10\text{ }\mu\text{m}$ sample areas were chosen from the 200- μm -diameter sample cavity. Sixteen Raman spectra from a 4×4 grid scan map were collected from each area. An average spectrum of the 64 spectra was then determined per pressure. Raman spectroscopy measurements were done at intervals of 2–3 GPa at room temperature.

As the Raman sampling areas in the center of the gasket cavity were in some proximity to the distribution of ruby balls,

the set pressure value was taken as the average of the various ruby ball fluorescence measurements. This yielded error bars of ± 0.5 GPa in the low pressure regime from the distribution of R_1 -line fluorescence values. At higher pressures a maximal relative error of $\pm 5\%$ was used for the set pressure value to take into account increasing levels of nonhydrostaticity due to the absence of any PTM. This relative error is a realistic estimate, based on similar Raman measurements under nonhydrostatic conditions at high pressure [16–18].

$^{11}\text{B}^+$ ions of 150 keV/ion at a fluence of 5×10^{12} ions/ cm^2 and beam current of $\sim 0.08\text{ }\mu\text{A}$ were used to prepare the implantation-preprocessed DWCNTs. The same probe and measurement protocols as for the reference sample were repeated in the HP Raman measurements on the implanted sample. Stopping distances for the $^{11}\text{B}^+$ ions were determined to be in the range 400–450 nm, using the SRIM computational program [19].

The Raman sampling depth for the 532-nm laser excitation wavelength was calculated to be 30 nm [20]. Implantation collision events are uniform to well beyond the Raman sampling depth (see the Supplemental Material [15], Sec. S2). The starting DWCNT loose powder sample was precompacted in the gasket cavity, giving a near mirror-flat sample suitable for implantation; this arrangement ensures preservation of shallow implanted surfaces after ion bombardment. Subsequent to implantation the gasket cavity was oriented in the DAC to ensure implanted surfaces faced the impinging shallow-probing Raman radiation.

Raman spectroscopy measurements at ultraviolet excitation wavelengths (UV-Raman) were done in search of the characteristic signature for sp^3 bonds. A Horiba LabRAM HR system employed in UV configuration was used to acquire all UV-Raman spectra reported in this study. The Horiba LabRAM HR system had an Olympus BX41 microscope attachment. The excitation laser source was a Lexel Model 95 SHG argon ion laser, at a wavelength of 244 nm. The sampling depth for the 244-nm laser excitation wavelength was ~ 14 nm. A ThorLabs $40\times$ UVB objective was used to focus the incident laser beam onto the sample. In addition, a 2400-lines per mm grating was used to disperse the backscattered light onto a liquid-nitrogen-cooled CCD detector. The data acquisition process was via LABSPEC v5 software. Laser power at sample was restricted to below 1 mW.

III. RESULTS AND DISCUSSION

The average representative Raman spectrum of the DWCNTs at ambient pressure, from 64 spectra, is shown in Fig. 1. The Raman bands are labeled RBMs (radial breathing modes), appearing in ranges 100–200 cm^{-1} , 220–300 cm^{-1} , and the range 320–500 cm^{-1} for a less distinct group of inner tubes), D (at 1352 cm^{-1}), G (at 1597 cm^{-1}), and the second order of the D band, G' (also known as the 2D band, at 2680 cm^{-1}). The RBMs were deconvoluted using a minimum number of Lorentzians to estimate some average tube diameters in the distribution. The tube diameter (d_t) was calculated using $\omega_{\text{RBM}} = \frac{227}{d_t} \sqrt{1 + (C \times d_t^2)}$ where ω_{RBM} is the RBM position and $C = 0.05786\text{ nm}^{-2}$, a constant catering for tube-to-tube and environmental interactions [21]. Thus, the diameters

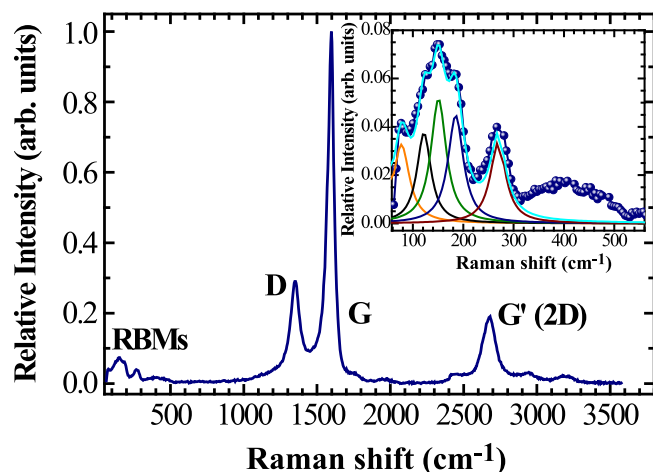


FIG. 1. Raman spectrum (average of 64 spectra) of the unimplanted sample at ambient pressure, with intensities normalized to the G band. Inset shows an example deconvolution of the RBMs using a minimum number of Lorentzians.

range from 0.9-nm inner tube average values, 1.3–2.1-nm outer and inner tube average values, up to 4.1-nm outer tubes, for corresponding wave-number ranges of $300\text{--}230\text{ cm}^{-1}$, $200\text{--}100\text{ cm}^{-1}$, and $<100\text{ cm}^{-1}$, respectively. The less distinct broad RBM feature in the range $500\text{--}320\text{ cm}^{-1}$ entails some inner tube diameters of $0.5\text{--}0.7\text{ nm}$.

Figures 2 and 3 show the evolution up to 20–25 GPa of *in situ* Raman spectra of reference and implanted samples, respectively. The general trend is characterized by an upshift in the D band position as well as broadening of the band as pressure increases. The G band features behave in a similar manner as those of the D band, and largely behave as reported for extensive work done on SWCNT bundles with [22–25] or without [8,26] pressure transmitting media.

To discern and quantify the spectral changes due to pressure, a deconvolution involving Lorentzians was effected on each of the spectra reported hereafter. Examples of these deconvolutions are shown in Figs. 2(b) and 3(b). The choice of Lorentzian line shape profile was made after different line shape functions (e.g., Gaussian function) were tried. The Lorentzian proved to be the best fitting function in this work, as was found in previous studies [8,18,22,25–27]. Useful parameters such as Raman band positions, linewidths, areas, and intensities were subsequently extracted from the best fittings for further analysis. To estimate errors, several fitting trials using different starting values of Lorentzian profile parameters were done, and spectral resolution and signal-to-noise ratio of the Raman spectra were also considered [16]. For example, we considered estimation of errors in Raman band parameters where there are overlapping peaks, as in the case of the position of the D band masked by the interfering adjacent diamond anvil peak; see Figs. 2 and 3.

A. Pressure evolution of D and G band positions for starting and implanted DWCNTs

Figure 4(a) shows the evolution of the D band position with pressure for the unimplanted sample. Within experimental uncertainty, as governed by the magnitude of the error bars and

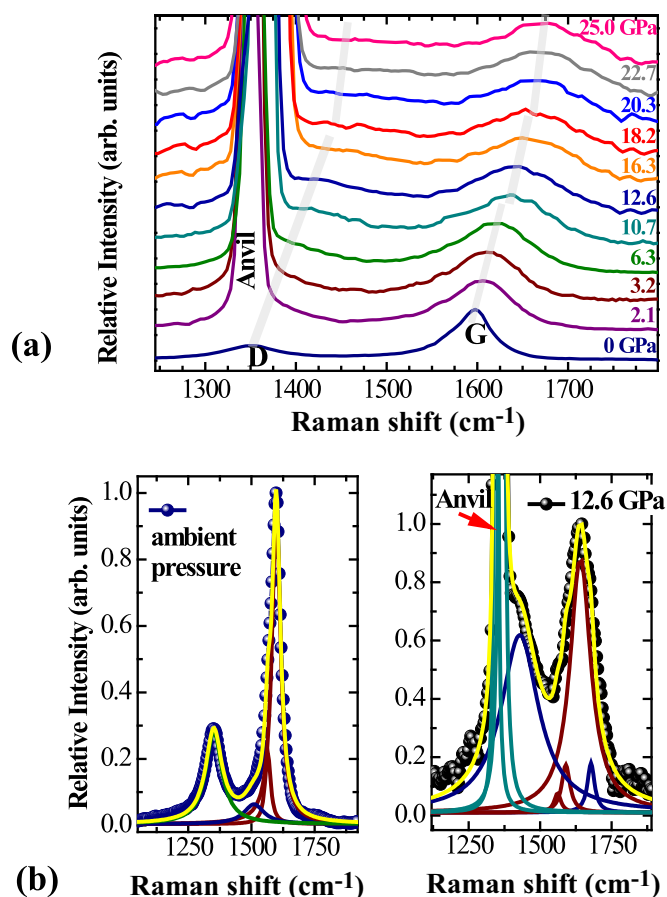


FIG. 2. (a) Compression sequence of Raman spectra of starting unimplanted DWCNTs in the range of characteristic D and G band signatures. The intense Raman signature appearing in the range $1332\text{--}1420\text{ cm}^{-1}$, for spectra collected at pressure other than ambient, is the first order peak of the diamond anvil. Spectra were collected at room temperature and normalized to the G band intensity. Faint bars to guide the eye, track intensity maxima from the spectral analysis, e.g., in (b), lower panels. (b) Left panel shows deconvolution of the spectrum acquired at ambient pressure, into respective components representing DWCNT Raman signatures. Two Lorentzians represent G^+ (1597 cm^{-1}) and G^- (1570 cm^{-1}) of the overall G band. Right panel has exemplary deconvolution of the spectrum acquired at 12.6 GPa. Assignment of the low intensity peaks is described in the text (Sec. III A).

as shown in Fig. 4(a), the D band position generally increases monotonically with pressure. The pressure dependence of the D band position over the range up to and including 18 GPa averages $\sim 5.6\text{ cm}^{-1}\text{ GPa}^{-1}$. There is a discontinuous change in the D band position in the vicinity of $\sim 18\text{ GPa}$ and above this there is a lower pressure dependence of $\sim 4.3\text{ cm}^{-1}\text{ GPa}^{-1}$.

Spectral parameters are more reliably obtained for the G band, which is well separated from the interfering diamond anvil peak, and is the band almost exclusively reported on in previous pressure studies of CNTs. Practically, only the G^+ component [8,25], the most intense tangential component of the G band, has been followed with change in pressure in earlier high pressure studies on CNTs [22,24,26]. At ambient pressure, the G^- component is of low intensity, appearing as

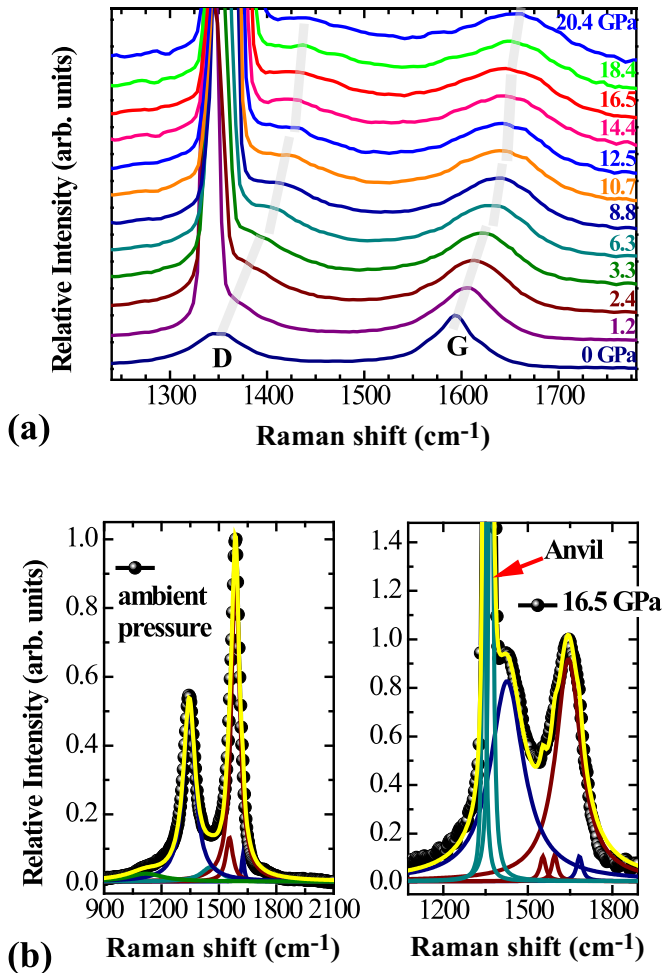


FIG. 3. (a) Compression sequence of the Raman spectra of implanted DWCNTs in the range of the characteristic D and G band signatures. Strong Raman signature appearing in the range $1332\text{--}1420\text{ cm}^{-1}$, for spectra at high pressure, is the first order peak of the diamond anvil. All spectra were collected at room temperature and normalized to the G band. Faint bars to guide the eye, track intensity maxima from the spectral analysis, e.g., in (b) lower panels. (b) Left panel shows deconvolution of spectrum at ambient pressure, into the respective components representing DWCNT Raman signatures. Two Lorentzians represent the G^+ (1588 cm^{-1}) and G^- (1560 cm^{-1}) of the overall G band. A D' band ($\sim 1625\text{ cm}^{-1}$) arises at ambient pressure (see Supplemental Material [15], Fig. S3). Right panel has exemplary deconvolution of the spectrum acquired at 16.5 GPa. Neglecting the low intensity peaks at 1555 and 1592 cm^{-1} leads to discrepancies in the cumulative fit compared with the data. These have the same origin as those of Fig. 2(b), described in the text.

a shoulder to the more intense G^+ component, with such a scenario being more pronounced in the case of DWCNTs. In addition, the G^- component is due to a pairwise in-plane vibration of atoms in a direction perpendicular to tube radius and tangential to the tube curvature. Hence, with increase in pressure comes a distortion of the oval nature of tubes, consequently decreasing the G^- contribution. Therefore, as pressure increases the parameters of the G^- component are less reliable. Hence, considering the above, only the G^+ component shall be used hereafter to represent the G band position

and intensity. The G band area shall, however, be comprised of both the G^+ and the G^- contributions.

For the unimplanted sample Fig. 2(b) shows exemplary fitting of a spectrum at 12.6 GPa to extract G -band parameters. The two components of the G band appear at positions 1640 cm^{-1} (G^+) and 1598 cm^{-1} (G^-). Neglecting the low intensity peaks at 1563 , 1598 , and 1675 cm^{-1} leads to discrepancies in the cumulative fit compared with the data. An additional peak emerges at $\sim 1675\text{ cm}^{-1}$ and is attributed to D' , a “defect” related feature [28], similar to the D band [29] in terms of intensity and area dependence on disorder in the graphitic hexagonal structure. Due to uniaxial stresses in the diamond of the anvil, the diamond first order peak splits into two components at high pressure, with positions at 1345 and 1366 cm^{-1} for the 12.6-GPa case reported in Fig. 2(b). The splitting was observed from ~ 9 GPa and above.

The positive pressure dependences of the G^+ band for the unimplanted sample are shown in Fig. 4(b). This is compared with the experiments on graphite by Hanfland *et al.* [30], presumably showing the expected maximum trajectory of the G band due to phonon hardening effects only, in an sp^2 bonded 2D network. Our DWCNT starting sample has a change in pressure dependence first at ~ 6 GPa where the initial $\sim 4.7\text{ cm}^{-1}\text{ GPa}^{-1}$ average slope changes to $3.4\text{ cm}^{-1}\text{ GPa}^{-1}$. The D to G intensity ratio in Fig. 5, discussed later in Sec. III C, also shows a drastic change in pressure dependence at ~ 6 GPa. More conspicuously, above ~ 18 GPa the G^+ band pressure dependence shows an appreciable change to a low near-plateau value of $0.3\text{ cm}^{-1}\text{ GPa}^{-1}$.

The evolution of the Raman signatures of implanted DWCNTs with pressure is strikingly different from the unimplanted DWCNTs, as emphasized in Figs. 4(c) and 4(d). Fitting protocols for the spectra are similar to the unimplanted sample, described above; see Fig. 3(b). Figure 4(c) shows the D band evolution with pressure for the implanted DWCNTs, and should be compared with the unimplanted case in Fig. 4(a). From ambient pressure to 3 GPa the pressure dependence is $10\text{ cm}^{-1}\text{ GPa}^{-1}$, and above this pressure the slope decreases appreciably to less than half the preceding value to attain a value of $3.3\text{ cm}^{-1}\text{ GPa}^{-1}$ beyond ~ 5 GPa.

By comparison of ambient pressure spectra reported in Figs. 2(b) and 3(b), the G band components, G^+ and G^- , shift to lower wave numbers after implantation by a magnitude of 9 and 10 cm^{-1} , respectively. These downshifts agree very well with earlier reports of Aitkaliyeva *et al.* [9] who observed a 10-cm^{-1} decrease in position of the G band components after irradiating MWCNTs with He ions of 150 keV/ion at a fluence of 10^{16} ions/cm^2 . Ion implantation results in momentum transfer from incident ions causing atomic displacements and in turn creating defects such as vacancies and adatoms [31]. The accumulation of defects on the surface of the CNTs results in the weakening of C-C bonds. In addition, vacancies can be stabilized by creation of Thrower-Stone-Wales (5-7-7-5) defects which results in varied force constants [10]. This leads to phonon softening in the pristine sp^2 -bonded lattice and associated downshifts in G band components [11,32].

Comparison of Figs. 4(b) and 4(d) shows that the evolution of the G^+ band with pressure for implanted DWCNTs has more conspicuous changes in pressure dependences, especially in the low pressure regime, than the unimplanted

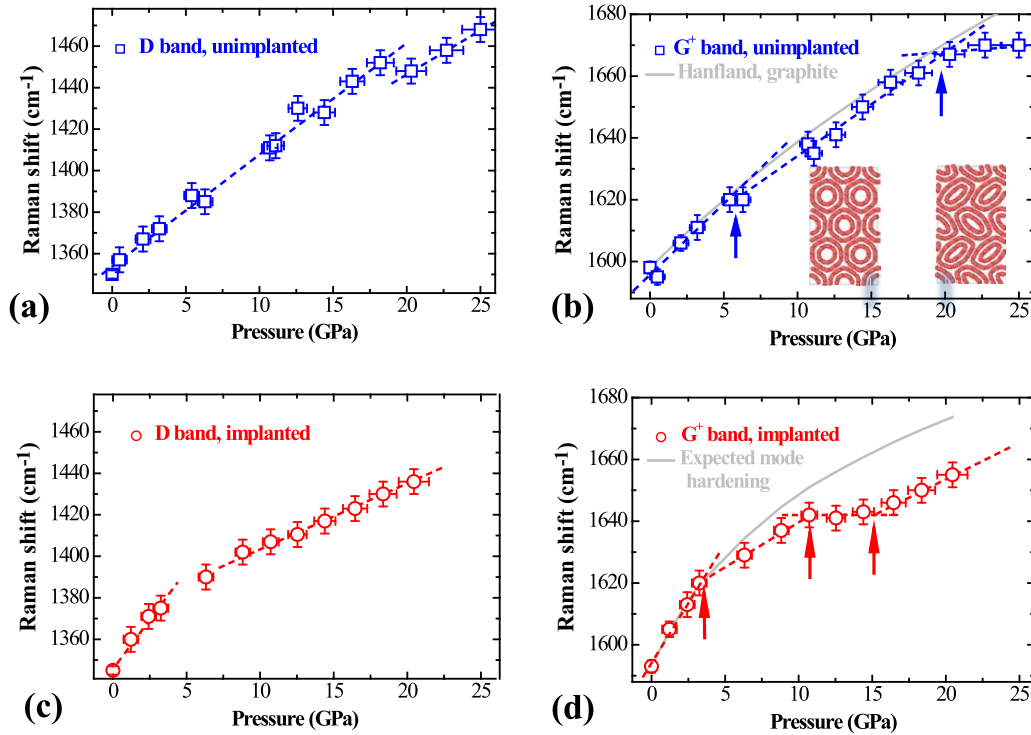


FIG. 4. (a) Evolution of D band position with pressure, for starting unimplanted DWCNTs. (b) Evolution of the G^+ band position with pressure, for the starting unimplanted DWCNTs. Grey solid line shows the expected maximum trajectory of the G band due to phonon hardening only, employing a model from graphite, after Hanfland *et al.* [30]. Insets show cross sections for pristine DWCNTs, obtained at 15 and 20 GPa from MD simulations, discussed in the text Sec. III B [15]. (c) Change in D band position with pressure for the implanted sample. (d) Change in G^+ band position with pressure for the implanted sample. Grey line shows expected trend due to normal mode hardening, based on extrapolated behavior of the low-pressure regime. In all panels dashed lines through the data guide the eye and arrows delineate where changes in pressure dependences (preceding average slope) occur for the well resolved G^+ band. Estimates of error bars are discussed at midway and start of Secs. II and III, respectively.

DWCNTs. Boundaries of the multiple-segment G^+ band evolution are marked by arrows in Fig. 4(d). For $0 \leq P \leq 3$ GPa, the pressure dependence of the G^+ position is

$\sim 7.9 \text{ cm}^{-1} \text{ GPa}^{-1}$, which drops to $\sim 3.0 \text{ cm}^{-1} \text{ GPa}^{-1}$ for $3 < P \leq 11$ GPa. The G^+ position tends to plateau in the range $11 < P \leq 14$ GPa, which is followed by an upturn in slope to $\sim 2.4 \text{ cm}^{-1} \text{ GPa}^{-1}$.

Subsequent discussion in the next Sec. III B ascribes the changes in pressure dependences of Figs. 4(b) and 4(d), to the deformation response of the initially circular DWCNT cross sections when they are under applied pressure.

B. Collapse pressures for reference and implanted DWCNTs

In comparison to SWCNTs under applied pressure, DWCNTs are expected to have added stability due to the presence of two tubes. There is a pressure screening effect from outer on inner tubes, whereby the outer tube acts as a protection shield and mechanical support for the inner tube [17,27,33,34]. In addition, with increase in pressure the two tubes tend to exhibit a strong coupling, with the inner tube acting as a structural support to the outer tube, which adds to an overall mechanical stability against pressurization [17,34,35].

Upon pressurization the initial radial cross section of CNTs evolves to high-curvature oval, peanut-shaped, or race-track conformations. The transition to these high-curvature cross-sectional profiles defines the geometrical collapse pressure P_c of the CNT [17,18]. A tube cross-section deformation sequence is typically from initially circular to

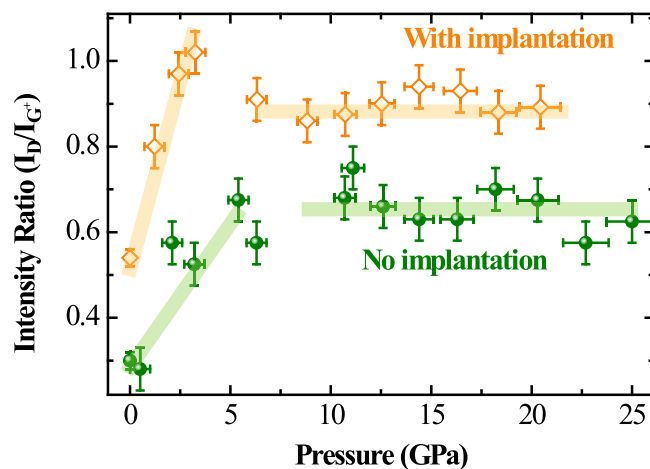


FIG. 5. Two-stage change in D to G^+ band intensity ratio with pressure. The faint bars are to guide the eye and delineate regimes of different pressure dependences discussed in the text (Sec. III C). Supplemental Material [15], Fig. S4, has the corresponding area ratios.

oval, then to polygonal (hexagonal) and then peanutlike or racetrack shapes. The shape-change sequence, however, depends on tube diameter. For example, a (10,0)@(18,0) DWCNT bundle has the following deformation sequence with pressure: circular-outer/circular-inner \rightarrow polygonal-outer/circular-inner \rightarrow polygonal-outer/oval-inner \rightarrow peanutlike-outer/oval-inner [34]. In spite of the possible multistep shape changes associated with different tube diameters, two main shape changes (circular \rightarrow polygonal or oval and polygonal or oval \rightarrow peanut or race-track) associated with two P_c values are discerned, with some DWCNT bundles only showing one higher P_c value associated with the collapse to a high-curvature peanut or race-track shape [18,34,36].

DWCNT cross-sectional changes under pressure are depicted by the insets in Fig. 4(b). These were obtained from molecular dynamics simulations, as described in the Supplemental Material [15], Sec. S5. The insets are for bundled (hexagonally packed) pristine (6,6)@(11,11) DWCNTs with inner (~ 0.8 nm) and outer (~ 1.5 nm) average diameters, similar to those responsible for the prominent RBM peaks in the inset of Fig. 1 for our starting sample. The insets in Fig. 4(b) show that polygonal-outer/circular-inner tubes are prevalent up to at least ~ 15 GPa and these have collapsed to racetrack-outer/oval-inner tubes by ~ 20 GPa.

Alencar *et al.* [18], have shown from theoretical considerations and experiments that in SWCNTs the transition pressure P_c is obtained from the Lévy-Carrier type law $P_c = (\frac{1}{d^3})\alpha(1 - \frac{\beta^2}{d^2})$ for tube diameters up to $d \sim 1.5$ nm, where $\alpha \approx 14$ GPa nm³ and $\beta \approx 0.5$ nm are numerical constants. According to Alencar *et al.* [18], the collapse pressure for DWCNTs also follows this formulation, except that inner tube considerations are most important and $d \equiv d_{\text{inner}}$ should be used in the above-mentioned Lévy-Carrier type formulation for P_c .

Considering the range of estimated diameters (0.9–4.1 nm) from the inset of Fig. 1, and the recent combined theoretical and experimental results of Alencar *et al.* [18], one can estimate the P_c value for the DWCNTs from the above-mentioned Lévy-Carrier type law. Some of the smallest inner tube diameters (~ 1 nm), e.g., deduced from the RBM wave-number range 230–300 cm⁻¹, would yield a corresponding P_c (inner) value of ~ 10 GPa [18,37]. Yet no major changes are discerned in the pressure dependences of Figs. 4(b) at ~ 10 GPa in the unimplanted reference case. A considerable change rather happens several GPa beyond this which we identify as $P_c \sim 18$ GPa. Alencar *et al.* [18] and Aguiar *et al.* [17], suggest that the outer tube offers chemical screening to the inner tube, whereas the inner tube guarantees mechanical support to the outer one, also suggested by Gadagkar *et al.* [38]. We invoke their arguments to explain why for our unimplanted DWCNTs P_c is several GPa beyond the ~ 10 GPa value obtained from considering the effects of d_{inner} alone in the Lévy-Carrier type formulation. Indeed Aguiar *et al.* [17] find that for DWCNTs with $d_{\text{outer}} = 1.56 \pm 0.54$ nm and $d_{\text{inner}} = 0.86 \pm 0.25$ nm, there are sequential collapses of outer and inner tubes at ~ 21 and 25 GPa, respectively.

Therefore in our unimplanted starting DWCNTs, the small change in pressure dependence of the G^+ band position at ~ 6 GPa in Fig. 4(b) is attributed to distortions in cross

section, from circular inner and outer tubes to circular inner tube and polygonal outer tube [17]. The more drastic change in pressure dependences at 18–20 GPa in Figs. 4(a) and 4(b) is attributed to DWCNT shape changes from the polygonal/circular outer/inner cross sections at low pressure to high-curvature oval inner tube and peanut or racetrack shaped outer tube [17,18]. Normally such collapse of the cross section results in plateauing of G -mode behavior [18,37], for which we see an onset at ~ 18 GPa in Fig. 4(b). This deformation sequence at low and high pressures is similar to what is depicted for the pristine DWCNTs in the insets of Fig. 4(b).

To identify the collapse pressure for the implanted DWCNTs, notice that the final segment above 14 GPa in Fig. 4(d) has a pressure dependence of ~ 2.4 cm⁻¹ GPa⁻¹, similar to the G band of graphite [30]. This final segment behavior and the preceding plateau behavior are typical signatures of CNT collapse [18,37]. The results of Figs. 4(c) and 4(d) for the implanted DWCNTs are suggestive of the anticipated initial change to circular inner tube and polygonal outer tube cross sections at ~ 3 GPa and at higher pressure, $P_c \sim 11$ GPa, collapse is likely to oval inner and racetrack or peanut profiled outer tubes [17].

Therefore, the main effect of the light-ion low-fluence implantation and consequent defect decoration of tube walls is to render some degree of mechanical softening of the implanted samples. This softening is seen in the steeper pressure dependence of the G -band frequencies in the initial stages of pressurization, $\partial\omega/\partial P \sim 8$ cm⁻¹ GPa⁻¹ for the implanted sample compared with $\partial\omega/\partial P \sim 5$ cm⁻¹ GPa⁻¹ for the unimplanted DWCNTs, in Figs. 4(b) and 4(d), respectively. The desirable effect of this softening is the alteration of deformation characteristics of the implanted tubes, such that collapse to high-curvature cross sections occur at lower threshold pressures ($P_c \sim 11$ GPa) than in starting unimplanted tubes ($P_c \sim 18$ GPa).

C. Defect proliferation in starting and implanted DWCNTs

Historically [39], the D to G band intensity ratio I_D/I_G has been the most useful parameter to characterize carbonaceous materials. The D band arises from a double resonance process that includes the elastic scattering of an electron (or hole) by defects. Such defects may include, but are not limited to, vacancies, divacancies, bond rotations forming 5-7-7-5 defects, grain boundaries, formation of dangling bonds, interstitials, formation of sp^3 intratube and intertube bonds, defect coalescence, and tube breakage [6,40]. These defects are either intrinsic from the DWCNTs synthesis procedures or may result from compression and implantation processing. We compare the I_D/I_G evolution under pressure for the reference and implanted samples in Fig. 5 to gain some insight into the defect proliferation, some of which may involve the sought after sp^3 interlinking.

It should be noted that at the low fluences of ¹¹B⁺ implantation used in our experiments (see Fig. S2 of the Supplemental Material [15]), the volume fraction of only vacancy defects, 1.2×10^{19} vacancies/cm³, would be well below 1%. Nevertheless, this low level of “point defect decoration” and the nature of any other cascading defect structures induced by such implantation seem to have an appreciable effect

on the pressure-induced defect proliferation, as suggested in Fig. 5.

Referring to Fig. 5, the D to G^+ band intensity ratio of the implanted DWCNTs at ambient pressure starts off at a higher value ($I_D/I_G \sim 0.54$) compared to the unimplanted sample ($I_D/I_G \sim 0.30$). This confirms that defect decoration of tube surfaces must have been realized in the implantation process. The I_D/I_G ratio for implanted DWCNTs rapidly increases with pressure reaching 1 by ~ 3 GPa, before developing a negative pressure dependence in the range 3–7 GPa, followed by a plateau regime of $I_D/I_G \sim 0.9$ up to the maximum pressure attained at 20.4 GPa. By comparison I_D/I_G for the unimplanted reference sample has an appreciably weaker positive pressure dependence up to 5–6 GPa, after which there is a change to plateau behavior at $I_D/I_G \sim 0.6$ or a weak negative pressure dependence up to ~ 25 GPa (see Fig. S5 of the Supplemental Material [15]).

Defect decoration in the implanted sample seems to facilitate the pressure-induced proliferation of additional defect structures, over and above what occurs in the unimplanted reference sample, as suggested by the difference in initial slopes in Fig. 5.

Both samples taken to the highest pressure and then decompressed and recovered to ambient conditions show appreciably enhanced I_D/I_G ratios compared to the start of pressurization, with the preservation of RBMs. This is depicted in Fig. 6 and discussed in the next Sec. III D. Figures 5 and 6 are compelling indications that additional defects, over and above what is already present at the outset at ambient conditions, are proliferated under pressure in both samples. However, as discussed in Sec. III D, with reference to the RBMs in Fig. 6(b) obtained in decompressed samples subsequent to pressurization, the proliferation of defect structures in tandem with the deformations and eventual collapse of the tubes under pressure does not lead to destruction of the DWCNTs.

It is more difficult to identify what defect structures, mentioned at the start of this subsection, evolve under pressure in the samples. However, as high pressure causes the DWCNTs to collapse from circular to high-curvature cross sections, this leads to an appreciable volume fraction of tube regions which are conducive to interlinking. Strain in the high-curvature parts of the collapsed DWCNTs induces rehybridization of the original sp^2 -hybridized orbitals to a configuration with greater sp^3 character [12], and this would be further facilitated at defect nucleation sites; see Fig. S7(a) of the Supplemental Material [15]. Furthermore, interstitial carbons from the implantation may offer a further contribution to the formation of tube interlinks. Existence of interstitial carbons has been demonstrated to enable formation of interlinks between the inner tube and a carbon chain encapsulated in a DWCNT upon pressurization [41].

Therefore, Figs. 4 and 5 are an indication that compared to ambient conditions, there is an enhanced defect density up to and beyond the pressure regimes where the tubes have collapsed to high-curvature cross sections (racetrack or peanut-shaped outer tubes) in both samples, i.e., ~ 18 GPa in the reference sample and ~ 11 GPa in the implanted sample. These drastic tube deformities are suitable scenarios for sp^3 interlinking [12], if this has not already been initiated at lower

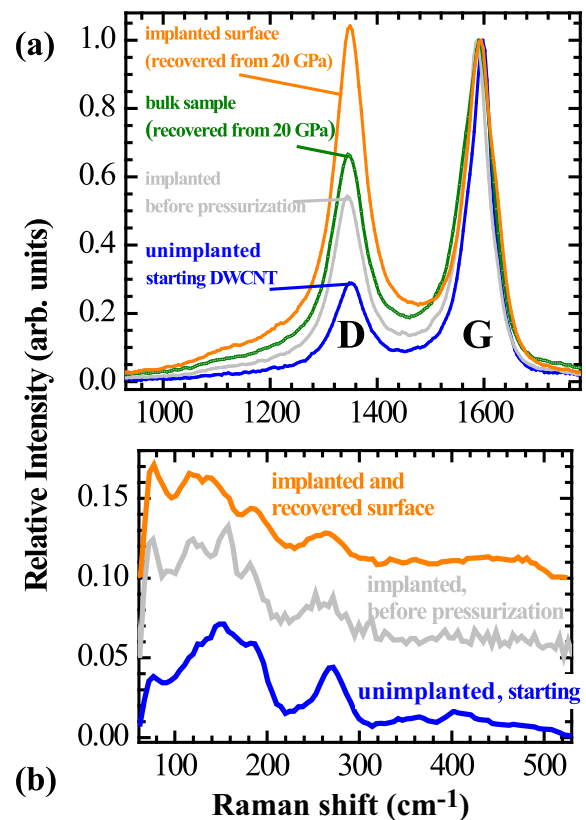


FIG. 6. (a) Raman spectra of reference and processed DWCNTs: unimplanted starting material (blue), implanted material before pressurization (grey), unimplanted and recovered from 20.4 GPa (green), and implanted and recovered from 20.4 GPa (orange). All spectra are normalized to the G band peak intensity. (b) Corresponding Raman spectra of (a) in the RBM region. All spectra are normalized to the G band. Spectra are displaced from one another by an equidistant gap for clarity.

pressures where there are less substantial tube cross-section changes (to polygonal outer and circular or oval inner tubes) [17,18].

D. Nature of samples recovered to ambient conditions from high pressure

The DAC involving implanted surfaces was decompressed from 20.4 GPa to ambient pressure in several steps. Upon opening the DAC, most of the regions of the implanted sample surface lifted off the sample cavity and remained adhered to the diamond anvil tip. Microscopic regions in the exposed sample cavity did not show adherence and liftoff. These were considered as exposed recovered implanted surfaces suitable for VIS- and UV-Raman probing. Figure 6 shows the Raman spectra of the samples recovered to ambient conditions from 20.4 GPa, for both implanted surface and unimplanted bulk regions.

Each of the spectra was well fitted with Lorentzian functions as described in the preceding sections. Relevant fitting parameters were extracted from the fitted spectra. Subsequent analysis was done, yielding additional parameters such as intensity and area ratios for the profiles in Fig. 6(a). In the

as-received DWCNT samples, implantation alone increases the I_D/I_G ratio from 0.3 to 0.5 and the corresponding area ratio from 0.5 to 0.8. On the other hand, the spectrum of the recovered sample after pressurization for implanted DWCNTs has a very high $I_D/I_G \sim 1$, while the corresponding area ratio shows an increase to 1.3.

The Raman spectra for the recovered samples in the RBM spectral range are shown in Fig. 6(b). The RBMs are still present in implanted DWCNTs compressed to ~ 20 GPa and then recovered to ambient conditions. Thus, tube integrity is largely preserved in the pressurization-decompression sequence. Noticeable in Fig. 6(b) are the changes in relative intensities of the RBMs as well as peak broadening after implantation and after both implantation and pressurization. These are attributed to nanotube interactions following implantation and pressurization of the DWCNT bundles. These interactions quench the 1D character of the electronic structure of the individual CNTs which, in turn, leads to a broadening of the sharp features in the electronic density of states and consequently reduce the resonant enhancement (intensity) of the Raman signal [4] and broaden the RBM features.

It is noteworthy that the I_D/I_G intensity ratios seem to be insensitive to resonance changes [25]. For example, in Fig. 6(b), RBM profiles for the implanted sample before and after pressurization are quite similar, implying minimal changes to resonance conditions. Yet there are appreciable changes in I_D/I_G ratios; see Fig. 6(a). This suggests that appreciably increasing I_D/I_G ratios from pressure are not necessarily due to changing resonance conditions, but are best ascribed to an irreversible increase in defect density under pressure up to 20 GPa. This increase in defect density has not radically altered the resonance signatures (RBM profiles). Furthermore, for a wider tube diameter range (inner and outer) under pressure, any losses of resonance conditions for a set of tube diameters is balanced by gains in resonance conditions as other tubes become resonant with the excitation laser; see Sec. S4 of the Supplemental Material [15].

We are primarily interested in whether some of the defect structures proliferated under pressure may involve sp^3 interlinking, also if defect decoration has facilitated this, and if these have occurred whether they are irreversible upon decompression to ambient conditions where there is a return to circular DWCNT cross sections. To this end UV-Raman spectroscopy is a relatively convenient probe. Higher laser excitation energies (~ 5 eV) at UV wavelengths have a much bigger Raman scattering cross section for sp^3 bonded carbon than Raman spectroscopy at visible wavelengths [42].

Although *in situ* UV-Raman measurements are not easy to implement at high pressure it is possible to take spectra of recovered regions of the sample, as presented in Fig. 7. This shows there is significant broadening of the spectrum for implanted and recovered samples in the D and G band regions. Background subtraction was done in the same way for all spectra.

There is a definite intensity above the baseline for the implanted and recovered material, starting at ~ 750 cm^{-1} [Fig. 7(b)]. Such signature intensity, especially in the 1100- cm^{-1} region, is normally considered indicative of sp^3 interlinking based on reported UV-Raman measurements of

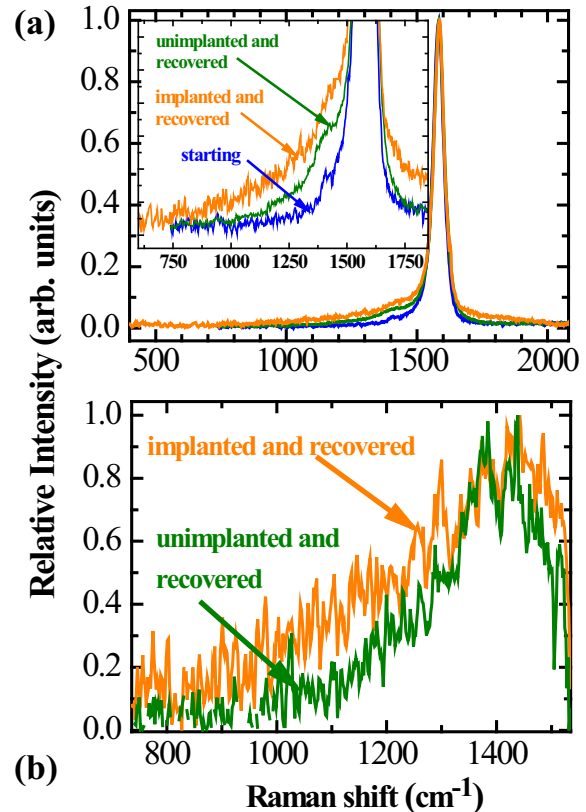


FIG. 7. (a) UV-Raman spectra of starting and processed DWCNTs measured using 244-nm laser excitation: starting DWCNT material (blue), unimplanted and recovered from 20.4 GPa (green), implanted and recovered (orange). The inset is a zoom-in to the region of interest. (b) The region of interest, after subtracting out the reference spectrum for starting DWCNTs from the spectra in (a).

sp^3 bonded systems [43,44]. Limited or low intensity enhancement at ~ 1100 cm^{-1} , similar to Fig. 7(b), is what would be expected for a low sp^3 volume fraction not exceeding a few %. This low sp^3 volume fraction would still be sufficient for an appreciable enhancement in mechanical properties of the DWCNTs without disruption to tube integrity [3]. At ~ 1400 cm^{-1} there is some D band contribution in Fig. 7(b).

On the other hand, the UV-Raman spectrum for the unimplanted and recovered sample does not show a significant feature in the region where an sp^3 signature is expected. A possible explanation is that if pressure-induced sp^3 interlinking is occurring then it is reversible upon pressure release in the unimplanted sample. There the intrinsic defect density in the reference tubes is not enough to, or the defects are of such a nature so as not to, generate any substantial irreversible sp^3 linkages between walls of tubes.

Light-ion low-fluence implantation decorates the tubes with isolated point defects, and there may be a cascade of other defect structures. It is reasonable to anticipate that these point defects and their dynamics assist in forming cross-wall linkages at high curvature regions of the deformed tube cross sections under pressure [12], seen in Fig. S7(a) of the Supplemental Material [15]. It is desirable to have further experimental corroboration of whether some of the irreversible

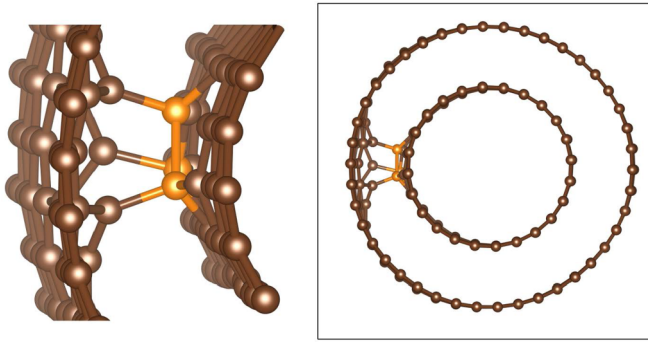


FIG. 8. One of the possible interlinks from MD simulations representing a DWCNT with a single vacancy on the outer tube yielding three sp^3 interlinks to the inner tube.

defect structures proliferated under pressure, exemplified in Figs. 6(a) and 7(b), are due to sp^3 interlinking, e.g., by electron energy loss spectroscopy (EELS) measurements [44].

To gain further insight into the stability of such point-defect-assisted sp^3 interlinks at ambient pressure, in samples recovered from high pressure when DWCNTs revert back to circular cross sections, we performed molecular dynamics (MD) simulations using the LAMMPS software package [45] and the ReaxFF_{C-2013} potential [46]. Further details are outlined in the Supplemental Material [15], Sec. S5.

A possible outer-to-inner tube intra-DWCNT link predicted by our MD simulations is shown in Fig. 8. Intra-DWCNT links have formation energies of 0.10, -0.23 , and -0.49 eV (-0.14 , -0.21 , and -1.21 eV) for one to three sp^3 bonds with respect to the nonlinked systems with a defect on the inner (outer) CNT, respectively (see Fig. 8). This trend is supported by MD simulations, which suggest that interlinks are stable for temperatures up to 800–1400 K, roughly correlated to the binding energy per atom. Inter-DWCNT links are less likely to occur naturally, as they are very sensitive to the position of the outer wall defect relative to where two neighboring DWCNT outer walls are nearest to each other (see Fig. S9, Supplemental Material [15]). They are, however, stable with formation energies of -0.57 , -1.15 , and -1.51 eV for one to three sp^3 bonds with respect to the nonlinked systems, respectively.

From these simulations it is concluded that sp^3 interlinking nucleated at vacancy sites from implantation would be highly stable in recovered samples at ambient pressure, where the DWCNTs revert to circular cross sections. These links likely involve multiple sp^3 bonds and are formed primarily from outer-to-inner walls (intra-DWCNTs), which would prevent “telescoping” effects under load. Inter-DWCNTs links are also stable but would be likely less abundant than intra-DWCNTs because of geometrical considerations.

IV. SUMMARY AND CONCLUSIONS

We show that even light-ion boron implantation at low fluences of 5×10^{12} ions/cm² of DWCNTs causes appreciable changes to the deformation characteristics and affect the

proliferation of defect structures under pressure. Comparison of Raman spectral parameters for unimplanted and implanted samples pressurised at room temperature to 20–25 GPa leads to the following conclusions:

(i) Circular-to-polygonal shape changes in tubular cross sections likely occur at ~ 3 GPa and ~ 6 GPa for unimplanted and implanted DWCNTs, respectively, as discerned from changes of pressure dependences of G -band frequencies, and I_D/I_G intensity ratios.

(ii) More drastic changes in pressure dependences of G -band frequencies at ~ 11 GPa for implanted DWCNTs and ~ 18 GPa for unimplanted DWCNTs are characteristic of full CNT collapse to flattened and high-curvature profiles (peanut-shaped or racetrack outer and oval inner tubes), consistent with theoretical and computational studies.

(iii) In the sample implanted at low fluences, defect production in the 30-nm sampling depth of the Raman probe likely involves mainly isolated point defects in the electronic stopping regime of the 150-keV $^{11}\text{B}^+$ ions. This level of less than 1% volume fraction of point defect decoration on tube surfaces and the nature of any other cascade of defect structures from the implantation does not extensively damage the DWCNTs. The RBM signatures in the spectra of pressurized samples recovered to ambient conditions corroborate this preservation of nanotube integrity.

(iv) The main effect of the light-ion low-fluence implantation and consequent defect decoration of tube walls is to render some degree of mechanical softening of the implanted samples. This softening manifests in the steeper pressure dependence of G -band frequencies in the initial stages of pressurization, ~ 8 cm⁻¹ GPa⁻¹ compared with ~ 5 cm⁻¹ GPa⁻¹ for the implanted and unimplanted DWCNTs, respectively. The desirable effect is alteration of deformation characteristics of the implanted tubes, such that high-curvature cross sections occur at lower threshold pressures than in unimplanted reference tube bundles, mentioned in (ii) above.

(v) The D to G^+ band intensity ratio, indicative of defect structures that alter the sp^2 bonding network, is enhanced in the implanted sample at the start of pressurization and has a much stronger pressure dependence than in the unimplanted sample in the low pressure regime. This is suggestive of irreversible defect structures being more readily proliferated in the implanted CNTs under compression subsequent to initial defect decoration.

Therefore light-ion low-fluence implantation preprocessing of CNTs is a potential route for altering their deformational and defect-proliferation characteristics under cold compression, without major disruptions to the integrity of the tubes. High curvature regions and enhanced defect proliferation in such deformed and implanted tube profiles under pressure make DWCNTs more amenable to having adjacent walls involve interlinking.

ACKNOWLEDGMENTS

The authors acknowledge Dr. G. Sauti (NASA Langley Research Center, USA) for the original idea and Dr. J. Changundega (UJ DFC, SA) for fruitful discussions in the formulation of the project. The support of the

DSI-NRF Centre of Excellence in Strong Materials (CoE-SM) and the CSIR African Laser Centre (Project No. LHIL500

Task ALC S100) towards this research is hereby gratefully acknowledged.

- [1] Q. Huang and L. Gao, Manufacture and electrical properties of multiwalled carbon nanotube/BaTiO₃ nanocomposite ceramics, *J. Mater. Chem.* **14**, 2536 (2004); V. N. Popov, Carbon nanotubes: properties and application, *Mater. Sci. Eng. R* **43**, 61 (2004); I. Ahmad, B. Yazdani, and Y. Zhu, Recent advances on carbon nanotubes and graphene reinforced ceramics nanocomposites, *Nanomaterials* **5**, 90 (2015).
- [2] A. Eatemadi, H. Daraee, H. Karimkhanloo, M. Kouhi, N. Zarghami, A. Akbarzadeh, M. Abasi, Y. Hanifehpour, S. W. Joo, and P. J. F. Harris, *Carbon Nanotube Science: Synthesis, Properties and Applications* (Cambridge University Press, New York, 2009).
- [3] Z. Xia, P. Guduru, and W. Curtin, Enhancing Mechanical Properties of Multiwall Carbon Nanotubes via sp^3 Interwall Bridging, *Phys. Rev. Lett.* **98**, 245501 (2007); A. F. Fonseca, T. Borders, R. H. Baughman, and K. Cho, Load transfer between cross-linked walls of a carbon nanotube, *Phys. Rev. B* **81**, 045429 (2010).
- [4] I. Loa, Raman spectroscopy on carbon nanotubes at high pressure, *J. Raman Spectrosc.* **34**, 611 (2003).
- [5] S. Saxena and T. A. Tyson, Interacting quasi-two-dimensional sheets of interlinked carbon nanotubes: A high-pressure phase of carbon, *ACS Nano* **4**, 3515 (2010); M. Huhtala, A. Krasheninnikov, J. Aittoniemi, S. Stuart, K. Nordlund, and K. Kaski, Improved mechanical load transfer between shells of multiwalled carbon nanotubes, *Phys. Rev. B* **70**, 045404 (2004); A. Kis, G. Csanyi, J.-P. Salvetat, T.-N. Lee, E. Couteau, A. Kulik, W. Benoit, J. Brugger, and L. Forro, Reinforcement of single-walled carbon nanotube bundles by intertube bridging, *Nat. Mater.* **3**, 153 (2004); M. Hu, Z. Zhao, F. Tian, A. R. Oganov, Q. Wang, M. Xiong, C. Fan, B. Wen, J. He, and D. Yu, Compressed carbon nanotubes: A family of new multifunctional carbon allotropes, *Sci. Rep.* **3**, 1331 (2013).
- [6] N. O'Brien, M. McCarthy, and W. Curtin, Improved intertube coupling in CNT bundles through carbon ion irradiation, *Carbon* **51**, 173 (2013).
- [7] B. Peng, M. Locascio, P. Zapol, S. Li, S. L. Mielke, G. C. Schatz, and H. D. Espinosa, Measurements of near-ultimate strength for multiwalled carbon nanotubes and irradiation-induced crosslinking improvements, *Nat. Nanotechnol.* **3**, 626 (2008).
- [8] S. Lu, M. Yao, Q. Li, H. Lv, D. Liu, B. Liu, R. Liu, L. Jiang, Z. Yao, and Z. Liu, Exploring the possible interlinked structures in single-wall carbon nanotubes under pressure by Raman spectroscopy, *J. Raman Spectrosc.* **44**, 176 (2013).
- [9] A. Aitkaliyeva, M. S. Martin, T. A. Harriman, D. S. Hildebrand, D. A. Lucca, J. Wang, D. Chen, and L. Shao, Radiation effects on the D to G Raman intensities of carbon nanotubes, *Phys. Rev. B* **89**, 235437 (2014).
- [10] S. Gupta and R. J. Patel, Changes in the vibrational modes of carbon nanotubes induced by electron-beam irradiation: Resonance Raman spectroscopy, *J. Raman Spectrosc.* **38**, 188 (2007).
- [11] U. Ritter, P. Scharff, C. Siegmund, O. P. Dmytrenko, N. P. Kulish, Y. I. Prylutsky, N. M. Belyi, V. A. Gubanov, L. I. Komarova, S. V. Lizunova *et al.*, Radiation damage to multiwalled carbon nanotubes and their Raman vibrational modes, *Carbon* **44**, 2694 (2006).
- [12] B. D. Jensen, J.-W. Kim, G. Sauti, K. E. Wise, L. Dong, H. N. Wadley, J. G. Park, R. Liang, and E. J. Siochi, Toward ultrahigh high-strength structural materials via collapsed carbon nanotube bonding, *Carbon* **156**, 538 (2020); R. Haddon, Chemistry of the fullerenes: The manifestation of strain in a class of continuous aromatic molecules, *Science* **261**, 1545 (1993); S. Reich, C. Thomsen, and P. Ordejon, Elastic properties and pressure-induced phase transitions of single-walled carbon nanotubes, *Phys. Status Solidi B* **235**, 354 (2003).
- [13] G. Y. Machavariani, M. P. Pasternak, G. R. Hearne, and G. K. Rozenberg, A multipurpose miniature piston-cylinder diamond-anvil cell for pressures beyond 100 GPa, *Rev. Sci. Instrum.* **69**, 1423 (1998).
- [14] E. Sterer, M. P. Pasternak, and R. D. Taylor, A multipurpose miniature diamond anvil cell, *Rev. Sci. Instrum.* **61**, 1117 (1990).
- [15] See Supplemental Material at <http://link.aps.org/supplemental/10.1103/PhysRevMaterials.5.033607> for computer simulation results of the $^{11}\text{B}^+$ implantation in carbon. There are further details of Raman characterization of starting DWCNTs sample, a plot of D to G band area ratio vs pressure, and a linear fit of D to G^+ intensity ratio of unimplanted DWCNTs for $P > 10$ GPa. The rationale on the insensitivity of D to G^+ band intensity ratio to resonance effects, for a wide DWCNT diameter distribution, is given. Further details of MD simulations are also given therein.
- [16] A. C. Torres-Dias, S. Cambré, W. Wenseleers, D. Machon, and A. San-Miguel, Chirality-dependent mechanical response of empty and water-filled single-wall carbon nanotubes at high pressure, *Carbon* **95**, 442 (2015).
- [17] A. L. Aguiar, E. B. Barros, R. B. Capaz, A. G. Souza Filho, P. T. C. Freire, J. M. Filho, D. Machon, C. Caillier, Y. A. Kim, H. Muramatsu *et al.*, Pressure-induced collapse in double-walled carbon nanotubes: chemical and mechanical screening effects, *J. Phys. Chem. C* **115**, 5378 (2011).
- [18] R. S. Alencar, W. Cui, A. C. Torres-Dias, T. F. T. Cerqueira, S. Botti, M. A. L. Marques, O. P. Ferreira, C. Laurent, A. Weibel, D. Machon *et al.*, Pressure-induced radial collapse in few-wall carbon nanotubes: A combined theoretical and experimental study, *Carbon* **125**, 429 (2017).
- [19] J. F. Ziegler, M. D. Ziegler, and J. P. Biersack, SRIM -The stopping and range of ions in matter, *Nucl. Instrum. Methods Phys. Res. B* **268**, 1818 (2010).
- [20] Y. W. Alsmeyer and R. L. McCreery, Surface-enhanced Raman spectroscopy of carbon electrode surfaces following silver electrodeposition, *Anal. Chem.* **63**, 1289 (1991).
- [21] P. T. Araujo, I. O. Maciel, P. B. C. Pesce, M. A. Pimenta, S. K. Doorn, H. Qian, A. Hartschuh, M. Steiner, L. Grigorian, K. Hata *et al.*, Nature of the constant factor in the relation between

- radial breathing mode frequency and tube diameter for single-wall carbon nanotubes, *Phys. Rev. B* **77**, 241403 (2008).
- [22] A. Merlen, N. Bendiab, P. Toulemonde, A. Aouizerat, A. San Miguel, J. L. Sauvajol, G. Montagnac, H. Cardon, and P. Petit, Resonant Raman spectroscopy of single-wall carbon nanotubes under pressure, *Phys. Rev. B* **72**, 035409 (2005).
- [23] C. Thomsen, S. Reich, H. Jantoljak, I. Loa, K. Syassen, M. Burghard, G. S. Duesberg, and S. Roth, Raman spectroscopy on single- and multi-walled nanotubes under high pressure, *Appl. Phys. A* **69**, 309 (1999).
- [24] U. D. Venkateswaran, E. A. Brandsen, U. Schlecht, A. M. Rao, E. Richter, I. Loa, K. Syassen, and P. C. Eklund, High pressure studies of the Raman-active phonons in carbon nanotubes, *Phys. Status Solidi B* **223**, 225 (2001).
- [25] A. J. Ghandour, D. J. Dunstan, A. Sapelkin, J. E. Proctor, and M. P. Halsall, High-pressure Raman response of single-walled carbon nanotubes: Effect of the excitation laser energy, *Phys. Rev. B* **78**, 125420 (2008).
- [26] S. Karmakar, S. Sharma, M. P. Teredesai, D. V. S. Muthu, A. Govindaraj, S. K. Sikka, and A. K. Sood, Structural changes in single-walled carbon nanotubes under non-hydrostatic pressures: X-ray and Raman studies, *New J. Phys.* **5**, 143 (2003).
- [27] R. S. Alencar, A. L. Aguiar, A. R. Paschoal, P. T. C. Freire, Y. A. Kim, H. Muramatsu, M. Endo, H. Terrones, M. Terrones, A. San-Miguel *et al.*, Pressure-induced selectivity for probing inner tubes in double- and triple-walled carbon nanotubes: A resonance Raman study, *J. Phys. Chem. C* **118**, 8153 (2014).
- [28] R. Tsu, J. H. González, and I. C. Hernández, Observation of splitting of the E_{2g} mode and two-phonon spectrum in graphites, *Solid State Commun.* **27**, 507 (1978).
- [29] M. S. Dresselhaus, A. Jorio, and R. Saito, Characterizing graphene, graphite, and carbon nanotubes by Raman spectroscopy, *Annu. Rev. Condens. Matter Phys.* **1**, 89 (2010).
- [30] M. Hanfland, H. Beister, and K. Syassen, Graphite under pressure: Equation of state and first-order Raman modes, *Phys. Rev. B* **39**, 12598 (1989).
- [31] A. Aitkaliyeva, M. C. McCarthy, M. Martin, E. G. Fu, D. Wijesundera, X. Wang, W.-K. Chu, H.-K. Jeong, and L. Shao, Defect formation and annealing kinetics in ion irradiated carbon nanotube buckypapers, *Nucl. Instrum. Methods Phys. Res. B* **267**, 3443 (2009).
- [32] P. Puech, E. Flahaut, A. Bassil, T. Juffmann, F. Beuneu, and W. S. Bacsa, Raman bands of double-wall carbon nanotubes: comparison with single- and triple-wall carbon nanotubes, and influence of annealing and electron irradiation, *J. Raman Spectrosc.* **38**, 714 (2007).
- [33] J. Arvanitidis, D. Christofilos, K. Papagelis, K. S. Andrikopoulos, T. Takenobu, Y. Iwasa, H. Kataura, S. Ves, and G. A. Kourouklis, Pressure screening in the interior of primary shells in double-wall carbon nanotubes, *Phys. Rev. B* **71**, 125404 (2005); G. A. Kourouklis, J. Arvanitidis, D. Christofilos, and S. Ves, High pressure Raman spectroscopy in carbon nanotubes, *Acta Phys. Pol. A* **116**, 13 (2009).
- [34] A. L. Aguiar, R. B. Capaz, A. G. Souza Filho, and A. San-Miguel, Structural and phonon properties of bundled single- and double-wall carbon nanotubes under pressure, *J. Phys. Chem. C* **116**, 22637 (2012).
- [35] J. Arvanitidis, D. Christofilos, K. Papagelis, T. Takenobu, Y. Iwasa, H. Kataura, S. Ves, and G. A. Kourouklis, Double-wall carbon nanotubes under pressure: Probing the response of individual tubes and their intratube correlation, *Phys. Rev. B* **72**, 193411 (2005).
- [36] X. Yang, G. Wu, and J. Dong, Structural transformations of double-walled carbon nanotube bundle under hydrostatic pressure, *Appl. Phys. Lett.* **89**, 113101 (2006).
- [37] S. Silva-Santos, R. Alencar, A. Aguiar, Y. Kim, H. Muramatsu, M. Endo, N. Blanchard, A. San-Miguel, and A. Souza Filho, From high pressure radial collapse to graphene ribbon formation in triple-wall carbon nanotubes, *Carbon* **141**, 568 (2019).
- [38] V. Gadagkar, P. K. Maiti, Y. Lansac, A. Jagota, and A. K. Sood, Collapse of double-walled carbon nanotube bundles under hydrostatic pressure, *Phys. Rev. B* **73**, 085402 (2006).
- [39] F. Tuinstra and J. L. Koenig, Raman spectrum of graphite, *J. Chem. Phys.* **53**, 1126 (1970).
- [40] J. H. Lehman, M. Terrones, E. Mansfield, K. E. Hurst, and V. Meunier, Evaluating the characteristics of multiwall carbon nanotubes, *Carbon* **49**, 2581 (2011); M. S. Dresselhaus and P. C. Eklund, Phonons in carbon nanotubes, *Adv. Phys.* **49**, 705 (2000); C. Caillier, D. Machon, A. San-Miguel, R. Arenal, G. Montagnac, H. Cardon, M. Kalbac, M. Zukulova, and L. Kavan, Probing high-pressure properties of single-wall carbon nanotubes through fullerene encapsulation, *Phys. Rev. B* **77**, 125418 (2008).
- [41] W. Neves, R. Alencar, R. Ferreira, A. Torres-Dias, N. Andrade, A. San-Miguel, Y. Kim, M. Endo, D. Kim, and H. Muramatsu, Effects of pressure on the structural and electronic properties of linear carbon chains encapsulated in double wall carbon nanotubes, *Carbon* **133**, 446 (2018).
- [42] M. Profeta and F. Mauri, Theory of resonant Raman scattering of tetrahedral amorphous carbon, *Phys. Rev. B* **63**, 245415 (2001).
- [43] A. C. Ferrari and J. Robertson, Resonant Raman spectroscopy of disordered, amorphous, and diamondlike carbon, *Phys. Rev. B* **64**, 075414 (2001); K. W. R. Gilkes, S. Praver, K. W. Nugent, J. Robertson, H. S. Sands, Y. Lifshitz, and X. Shi, Direct quantitative detection of the sp^3 bonding in diamond-like carbon films using ultraviolet and visible Raman spectroscopy, *J. Appl. Phys.* **87**, 7283 (2000); V. Merkulov, J. Lannin, C. Munro, S. Asher, V. Veerasamy, and W. Milne, UV Studies of Tetrahedral Bonding in Diamondlike Amorphous Carbon, *Phys. Rev. Lett.* **78**, 4869 (1997).
- [44] M. Hu, J. He, Z. Zhao, T. A. Strobel, W. Hu, D. Yu, H. Sun, L. Liu, Z. Li, and M. Ma, Compressed glassy carbon: An ultra-strong and elastic interpenetrating graphene network, *Sci. Adv.* **3**, e1603213 (2017).
- [45] S. Plimpton, Fast parallel algorithms for short-range molecular dynamics, *J. Comput. Phys.* **117**, 1 (1995); H. M. Aktulga, J. C. Fogarty, S. A. Pandit, and A. Y. Grama, Parallel reactive molecular dynamics: Numerical methods and algorithmic techniques, *Parallel Comput.* **38**, 245 (2012).
- [46] A. C. T. van Duin, S. Dasgupta, F. Lorant, and W. A. Goddard, ReaxFF: A reactive force field for hydrocarbons, *J. Phys. Chem. A* **105**, 9396 (2001); S. G. Srinivasan, A. C. T. van Duin, and P. Ganesh, Development of a ReaxFF potential for carbon condensed phases and its application to the thermal fragmentation of a large fullerene, *ibid.* **119**, 571 (2015).